Available online at www.sciencedirect.com
ScienceDirect
Journal of Computational Physics 227 (2008) 6944–6966
JOURNAL OF COMPUTATIONAL PHYSICS
www.elsevier.com/locate/jcp

The XTOR code for nonlinear 3D simulations of MHD instabilities in tokamak plasmas

Hinrich Lütjens *, Jean-François Luciani

Centre de Physique Théorique, Ecole Polytechnique, CNRS, France

Received 8 October 2007; received in revised form 11 March 2008; accepted 4 April 2008
Available online 15 April 2008

Abstract

The latest version of the XTOR code which solves a set of the extended magnetohydrodynamic (MHD) equations in toroidal geometry is presented. The numerical method is discussed with particular emphasis on critical issues leading to numerical stability and robustness. This includes the time advance algorithm, the choice of variables and the boundary conditions. The physics in the model includes resistive MHD, anisotropic thermal diffusion and some neoclassical effects. The time advance method used in XTOR is unconditionally stable for linear MHD. First, both the ideal and the resistive MHD parts of the equations are advanced semi-implicitly and then the thermal transport part full-implicitly, using sub-stepping [H. Lütjens, Comp. Phys. Commun. 164 (2004) 301]. The time steps are only weakly limited by the departure of the nonlinear MHD dynamics from the linear one and are automatically defined by a set of nonlinear stability criteria. The robustness of the method is illustrated by some numerically difficult simulations, i.e. sawtooth simulations, the nonlinear destabilization of ballooning instabilities by an internal kink, and the dynamics of a neoclassical tearing mode in International Thermonuclear Experimental Reactor (ITER) [R. Aymar, V.A. Chuyanov, M. Huguet, et al., Nucl. Fusion 41 (2001) 1301] like geometry about its nonlinear stability threshold.

PACS: 52.55.Xz; 52.30.−q; 52.30.Cv; 52.35.Mw; 52.35.Py; 52.55.Fa; 52.55.Tn; 52.65.−y; 52.65.Kj

Keywords: Plasma; Tokamak; Magnetohydrodynamics; Nonlinear simulations; Semi-implicit; Internal kink; Ballooning instability; Tearing mode

1. Introduction

In high performance tokamaks the plasma is stable towards the most dangerous ideal magnetohydrodynamic (MHD) instabilities, e.g. current driven external kinks, even if the margin is weak in some cases. A future fusion reactor must of course be operated in windows which are linearly stable towards these classes of instabilities.

* Corresponding author. Tel.: +33 169334236; fax: +33 169334949.
E-mail address: Hinrich.Lutjens@cpht.polytechnique.fr (H. Lütjens).

0021-9991/$ - see front matter © 2008 Elsevier Inc. All rights reserved.
doi:10.1016/j.jcp.2008.04.003

But in these operating regimes the plasma is exposed to other macro-instabilities such as, e.g. the internal $m/n = 1/1$ kink mode [3,4] or tearing instabilities which typically grow on a resistive (i.e. slow) time scale (m and n are the poloidal and the toroidal mode number, respectively). They can be linearly or nonlinearly unstable. In the latter case, they need a finite magnetic seed island to grow, as e.g. the neoclassical tearing modes (NTM). It is believed that such seed islands are provided by other instabilities such as, e.g. internal kinks or edge localized modes (ELMs).

In some cases, these macro-instabilities only cause a partial plasma de-confinement and in others they can lead to the loss of the discharge. Consequently, the understanding of their dynamics is a crucial issue for high performance tokamaks. It will allow to choose between several options: (a) avoiding them by tuning the physical parameters of the discharges, (b) stabilizing them with external sources (antennas, gyrotrons, etc.) or (c) if their effect on the confinement is weak possibly living with them. Assimilating this knowledge is at moment one of the key issues in the tokamak research field and it has been the main drive in the development of the XTOR code.

At lowest order, these instabilities are governed by resistive MHD, but the proximity of their stability thresholds makes them sensitive to many higher order physical effects. Moreover, their dynamics in the torus differs significantly from the one in the slab or the cylinder because of their sensitivity to pressure effects. Therefore, the essential objectives in developing XTOR were to solve the full MHD equations in toroidal geometry and to structure the code to facilitate future modifications which are, e.g. a new time stepping scheme or adding more physics to the model.

The first numerical studies of the evolution of MHD instabilities were performed about 30 years ago. The computer power at that time was limited and in order to make the solution of the problem tractable, the compressible fast magneto-sonic waves were removed from the spectrum by solving the reduced MHD equation [5,6] or by assuming incompressibility [7]. In the former method, toroidal effects were included by the addition of large aspect ratio corrections to the model [8–10]. The time advance scheme in these codes was explicit and thus limited by a Courant–Friedrich–Levy (CFL) condition on the time step, $\Delta t < \tau_a/m_{max}$ where τ_a is the toroidal Alfvén time ($\tau_a = R_0/v_a$, where R_0 is the major axis of the torus and $v_a = B/\rho^{1/2}$ is the Alfvén velocity) and m_{max} the highest poloidal mode in the simulation. This CFL condition is very stringent for long time three-dimensional full MHD simulations, and can only be circumvented entirely by a fully implicit time stepping scheme with the disadvantage that very large matrix systems must be solved at every time step.

At the end of the 1980's, solving the three-dimensional full MHD problem implicitly was a rather formidable task with the then existing computers. Amongst other methods used by Aydemir and Barnes [11], Park et al. (M3D) [12] and Popov et al. (NFTC) [13], a very fruitful attempt was the solution using semi-implicit methods first proposed by Harned and Kerner [14] and Harned and Schnack [15,16]. The goal was to reach numerical stability using tools much simpler than fully implicit schemes. This was achieved by using algebraically simplified operators, see Section 3.1.1. The first code of this category was the FAR code [17] which handled the linearized MHD stability part of the equations implicitly and damped the fast magneto-sonic waves by the addition of an explicit diffusive term. This idea was refined iteratively [14–16,18] by developing numerically stabilizing operators which play the role of a low frequency filter to get rid of the diffusive term in Ref. [17]. These works progressively revealed that the most efficient semi-implicit operator is the linearized second-order MHD operator. This was the choice for XTOR [18].

The NIMROD code was developed more recently [19] and uses a time advance very similar to the one of XTOR. The main difference is that NIMROD uses a finite element representation in the poloidal plane whereas XTOR uses Fourier transforms in all the angular directions. As a consequence NIMROD can be applied to the whole plasma domain including a separatrix. On the other hand, the linear algebra is much more efficient with XTOR for the same spectral content.

Early tests done in Ref. [18] have revealed the robustness of this semi-implicit method for internal kink and tearing mode simulations. This motivated a line of development of semi-implicit full MHD codes which resulted in the XTOR code described in the present work. It uses a semi-implicit time advance scheme slightly different from the one in Ref. [18], see Section 3.2. The particularity of this scheme is the fully implicit treatment of the linear ideal MHD part of the equations. Only the departure of the nonlinear MHD dynamics from the linear one is explicit, resulting in a time step reduction. But the time step remains much larger than the one

of a fully explicit time advance scheme, even in the nonlinear phase of the evolutions of the instabilities. The non-ideal MHD parts of the equations are stepped forward in time with a separate sub-step [1].

In the first version of XTOR the equilibrium poloidal magnetic flux surfaces were approximated as non-concentric circles (shifted outward by the so-called "Shafranov shift"). This version of the code was limited in the plasma geometry and restricted to plasma equilibria with a very small Shafranov shift. The resolution of resonant surfaces with an elliptic poloidal cross-section is indeed difficult by this method. This is even true for circular equilibria with a large Shafranov shift because of the ellipticity of the resonant surfaces in the core region of the plasma. Nevertheless this precursor version of XTOR was used for the first time for a quantitative study of the nonlinear behavior of the resistive MHD dynamics of the $m = 1/n = 1$ internal kink dynamics in the torus [20]. In this work, the simulations allowed the achievement of a quantification of the stochasticity near the $q = 1$ surface induced by the magnetic reconnection.

In order to get rid of the geometric limitations of the initial version of XTOR, the code was deeply modified mid of the 1990's to allow plasma simulations with an initial equilibrium solution provided by the CHEASE code [21,22]. Magnetic flux coordinates were introduced in the direction of the small radius of the torus combined with a non-diagonal metric in the poloidal plane. As a consequence, co- and contra-variant representations of the fields had to be used. These representations have been implemented with a special care to keep the self-adjointness property of the ideal MHD problem. The increasing complexity of the algebra compelled us to construct the matrices of the linear operators column-wise, computing the image of basis functions by the linear operator. This automatizes the matrix constructions to a certain level, reduces coding error sources and allows an easier implementation of effects generalizing the MHD model. This resistive MHD version of XTOR was used to study quantitatively the nonlinear destabilization of moderate-n ballooning modes by internal kink instabilities [23].

Subsequently, the physical model in XTOR was improved by the inclusion of an anisotropic thermal diffusion and a bootstrap current term. As for the ideal MHD part, a particular attention was paid to the self-adjointness of the discretized anisotropic transport operator. As for the resistive MHD part of the equations, the time advance of the thermal transport part is separated in a sub-step. It is fully implicit and uses a preconditioned conjugate gradient method.

This version of the code has been used extensively for the study of the dynamics of standard and neoclassical tearing instabilities in ITER [2] like geometries [24–28] and experimental TORE-SUPRA discharges [29,30]. In order to address these difficult problems, the numerical scheme must be able to solve a large time scale range. For example, growth rates of tearing instabilities with a plasma resistivity of $\eta = 10^{-7}$ are of the order of 10^{-5}–$10^{-4}\tau_a^{-1}$, requiring time evolutions of the order of 10^5–$10^6\tau_a$ for a complete picture of their dynamics. Conversely, the frequency of compressional Alfvén modes in the discretized spectrum (upper limit of the discretized spectrum) near the mesh axis can be up to $10^4\tau_a^{-1}$. Therefore, the overall stiffness of the problem is about 10^{10}.

The present paper is organized as follows. In Section 2, we mention the equations solved by XTOR. The numerical method used for this purpose is presented in Section 3. The key issues consisting of the choice of the time stepping algorithm and its linear and nonlinear numerical stability properties, the choice of variables and the setting of the boundary conditions are addressed. As applications we show in Section 4: (a) the time evolution of internal kink oscillations, (b) the nonlinear destabilization of moderate n ballooning instabilities by an internal kink and (c) the evolution of a neoclassical tearing mode about its nonlinear stability threshold. Last, future developments are suggested as conclusions in Section 5.

2. Physics

XTOR solves the full resistive MHD equations including anisotropic thermal transport and some neoclassical effects. The velocity, the magnetic and the pressure fields $\mathbf{v}$, $\mathbf{B}$ and p, respectively, are simultaneously advanced in time. As an option, it is possible to split the pressure advance into temperature T and density ρ advance. The equation set solved is

$$\begin{aligned} \rho\partial_t\mathbf{v} &= -\rho(\mathbf{v}\cdot\nabla)\mathbf{v} + \mathbf{J}\times\mathbf{B} - \nabla p + \nabla\nu\nabla\mathbf{v} \\ \partial_t\mathbf{B} &= \nabla\times(\mathbf{v}\times\mathbf{B}) - \nabla\times\eta(\mathbf{J}-\mathbf{J}_{\mathrm{boot}}) \end{aligned} \tag{1}$$

with

$$\begin{aligned} \partial_t p &= -\Gamma p \nabla \mathbf{v} - \mathbf{v}\cdot\nabla p + \nabla \rho\chi_\perp \nabla \frac{p}{\rho} + \nabla\cdot\left[\mathbf{B}\left(\frac{\rho\chi_\parallel}{B^2}(\mathbf{B}\cdot\nabla)\frac{p}{\rho}\right)\right] + H \\ \rho &= Cp^{-\Gamma} \end{aligned} \tag{2}$$

or

$$\begin{aligned} \partial_t T &= -(\Gamma-1)T\nabla\mathbf{v} - \mathbf{v}\cdot\nabla T + \frac{1}{\rho}\nabla\rho\chi_\perp\nabla T + \frac{1}{\rho}\nabla\cdot\left[\mathbf{B}\left(\frac{\rho\chi_\parallel}{B^2}(\mathbf{B}\cdot\nabla)T\right)\right] + H \\ \partial_t \rho &= -\rho\nabla\mathbf{v} - \mathbf{v}\cdot\nabla\rho + \nabla D_\perp\nabla\rho + S \end{aligned} \tag{3}$$

The geometry of the plasma is toroidal with non-circular poloidal cross-sections. At present, the code has fixed boundary conditions. It requires a perfectly conducting shell at the plasma surface. Moreover, it cannot handle equilibria with a plasma separatrix inside the domain of solution.

In the set of equations solved by XTOR, $\mathbf{J} = \nabla\times\mathbf{B}$ is the current density field. v and η are plasma viscosity and resistivity fields, respectively. In the transport terms of the evolution of p, T and ρ, $\chi_\perp$, $D_\perp$ and $\chi_\parallel$ are the perpendicular and parallel diffusion coefficients. H and S are the heat and density sources, respectively. In general, there is no parallel diffusion density coefficient in transport models. It could be included into Eq. (3) if necessary. Γ is the ratio of specific heats. XTOR uses a simplified version of the bootstrap current density given by $\mathbf{J}_{\mathrm{boot}(\mathbf{t})} = f_{\mathrm{bs}}\|\mathbf{J}_{\mathrm{boot},0}\|(\nabla p(t))_r/p_0'\mathbf{B}(\mathbf{t})/\|\mathbf{B}(\mathbf{t})\|$. It follows in time the evolution of the magnetic field line topology through the parallel dynamic of the pressure. The factor f_{bs} is a numerical factor, which accounts for the nonlinear effects in the bootstrap current. Experimental fits give $f_{\mathrm{bs}}\approx 0.7$ as a reasonable approximation [31]. $\|\mathbf{J}_{\mathrm{boot},0}\|$ is computed in toroidal geometry by the CHEASE equilibrium code [21,22]. If ρ and T evolve separately, the bootstrap current density is formed by a density and a temperature contribution [32].

The normalizations chosen in XTOR are as follows (see [22, Section 5.4.4]). $a = 1$, where a is the half size of the plasma cross-section in the $Z = 0$ symmetry plane. This is consistent with the metrics imported from the CHEASE code. Therefore the magnetic axis is defined by the dimensionless number R_0. The magnetic field unity is set by $B_{\phi,0} = R_0$. Therefore, if ρ is normalized to its central value ρ_0 the time unit is the Alfvén time $\tau_a = (\mu_0\rho_0)^{1/2}R_0/B_0$, i.e. the Alfvén time defined from the toroidal field and the major radius or equivalently from the magnetic field unit and the length unit. In this normalization, the Lundquist number is the inverse of the resistivity, i.e. $S = \eta^{-1}$.

In the simulations, η varies in time according to Spitzer's resistivity law $\eta\propto T^{-3/2}$. This evolution is initialized by a mapping between equilibrium resistivity and temperature (or pressure if ρ is adiabatic). This mapping is then used at every time step to evaluate $\eta(T(t))$. The initial η profile is obtained by the resistive equilibrium constraint demanding $\eta_0\langle(J_{\Phi,0} - J_{\Phi,\mathrm{boot},0})\rangle = E_{\Phi,0}$ to be constant. $E_{\Phi,0}$ is then imposed as a boundary condition on the toroidal electric field throughout the entire simulation to maintain the $n = 0$ components of the fields in place.

The transport coefficients $\chi_\perp$, $D_\perp$ and $\chi_\parallel$ can be non-constant provided that the diffusive terms in Eqs. (2) and (3) are self-adjoint. In principle, they could be given by a micro-turbulence model or experimental measures. In the test cases presented in Section 4, $\chi_\perp$ is constant for the sawtooth example and proportional to the resistivity η for the other cases. For all three examples, $\chi_\parallel$ is constant.

3. Numerical method

3.1. The semi-implicit time advance schemes

In three-dimensional tokamak MHD, the interest is focussed on low frequency instabilities in the framework of equations which describe magnetic compressional waves as well. The latter issue excludes the use of explicit methods in practice. The first ideas to handle this problem lead to the use of semi-implicit methods, first proposed by Harned–Kerner [14] and Harned–Schnack [15,16] in the context of magnetic fusion.

3.1.1. Application to a set of nonlinear oscillators

Semi-implicit methods can easily be introduced by a comprehensive example, although different from the historical development. Consider a set of nonlinear oscillators described by the following equations,

$$\begin{aligned} \dot{X} &= V \\ \dot{V} &= -LX + NL(X)X \end{aligned} \tag{4}$$

where X and V are N-dimensional vectors. The dots denote time derivatives. The eigenvalues of L are the normal modes of the problem. It can be supposed that the spectrum of L leads to a stiff problem, similar to MHD, i.e. there is a coexistence of "small" and "large" eigenvalues and only the small ones are involved in the physics of interest. The matrix $NL(X)$ contains the nonlinearities and vanishes for $X \to 0$.

This set of equations can be solved by the so-called "leapfrog" scheme

$$\begin{aligned} X_{n+1/2} - X_{n-1/2} &= \Delta t V_n \\ V_{n+1} - V_n &= -\Delta t L X_{n+1/2} + \Delta t NL(X_{n+1/2}) X_{n+1/2} \end{aligned} \tag{5}$$

where n indexes the time step. A first semi-implicit scheme results from the modification of (5) into

$$\begin{aligned} X_{n+1/2} - X_{n-1/2} &= \Delta t V_n \\ V_{n+1} - V_n &= -\frac{\Delta t}{2} L(X_{n+3/2} + X_{n-1/2}) + \Delta t NL(X_{n+1/2}) X_{n+1/2} \end{aligned} \tag{6}$$

This scheme can also be characterized as "linearly implicit" and "nonlinearly explicit", corresponding to the time advance choice for the linear and nonlinear quantities, respectively.

By simple algebra, Eq. (6) can be transformed into

$$\begin{aligned} X_{n+1/2} - X_{n-1/2} &= \Delta t V_n \\ (1 - \Delta t^2 L)(V_{n+1} - V_n) &= -\Delta t L X_{n+1/2} + \Delta t NL(X_{n+1/2}) X_{n+1/2} \end{aligned} \tag{7}$$

It is easy to check that this scheme is (linearly) unconditionally stable for every time step. The structure of the original explicit leapfrog scheme is recovered. The semi-implicit operator, which appears in the left-hand side of (7), has obviously the same spectrum as L. It acts as a "mass matrix" which reduces the frequency of the fastest mode to an effective frequency of order Δt^{-1}. This effective frequency turns out to be in the stable part of the original explicit leapfrog scheme.

Starting from this simple scheme, two major extensions lead to semi-implicit methods used in previous works in magnetic fusion.

3.1.2. Changes of the linear semi-implicit operator

In practice, the full semi-implicit operator can be lengthy to invert. As in the original Harned–Schnack method, it can be replaced by another semi-implicit operator,

$$I - \Delta t^2 L \to I - G \tag{8}$$

If G is "larger" than $\Delta t^2 L$, the new mass matrix also leads to numerical unconditional stability. But the drawback is that the eigenvectors are no longer preserved. In MHD, the low frequency modes generally exhibit very localized structures, near resonant surfaces. And the slower they are, the more localized they are, too. Therefore, sufficient spacial accuracy requires a rather small time step in order to avoid a too large mode distortion by the mass matrix. It is the reason why, in Ref. [18] the use of the exact linearized MHD operator was proposed for XTOR. The same choice was done for NIMROD in Ref. [19] for instance. In XTOR, the inversion and storage is not expensive computationally, due to the spectral representation, see Section 3.6. In NIMROD, due to finite elements, the inversion is more difficult.

The nonlinear equations, solved in Eq. (7), can lead to numerical instability, due to nonlinear terms coming from $NL(X)$. Therefore another improvement is the addition to L of an operator that overcomes the nonlinear part, again using a "mass matrix". This strategy is employed in XTOR to deal with nonlinear radial magnetic field coming from MHD modes, as discussed in Section 3.4.

3.1.3. Changes of the numerical explicit scheme

MHD is a Hamiltonian problem, but it cannot be written in the simple form (4). Thus the simple leapfrog scheme cannot be used. For instance, the magnetic convection has to be treated carefully. In Harned–Kerner, a two step predictor–corrector was used. The same numerical scheme was used in Ref.[18]. Here, in the present version of XTOR, a new scheme is presented, as described in Section 3.2.

For these more complicated schemes, the derivation of a semi-implicit scheme from an explicit one by simple time shifts, as in Eq. (7), is not possible in general. A semi-implicit scheme is then defined as an underlying explicit scheme, with a numerical stabilization coming from the application of a "mass matrix" to the velocity equation.

In XTOR, this "mass matrix" is again the exact linearized MHD stability operator (modified by the addition of a Laplacian term for nonlinearities),

$$\text{Mass matrix} = I - \alpha\Delta t^2 L_0 - c\nabla^2 \equiv I - G. \tag{9}$$

With this choice, generally, for a given underlying explicit scheme, there is a critical α which ensures linear unconditional stability. The use of a value of α larger than this threshold does not lead to numerical distortion, because the mass matrix preserves the physical eigenvectors (if c is sufficiently small). On contrary, it can provide a numerical margin that is exploited in XTOR for nonlinear stability assessment, see Section 3.4.

3.2. Time advance method of the ideal MHD part

The time stepping scheme presented in Ref. [18] for the ideal MHD part of the dynamics was based on a method proposed in Refs. [14,15] which required a semi-implicit step for both the predictor and the corrector. It appears that the same numerical performance can be achieved with only one semi-implicit step by using a multi-step predictor-corrector defined as follows:

Predictor:

$$\begin{aligned} b^* &= \frac{b_n + b_{n-1}}{2} + \Delta t F_b(v_n, b_n) \\ p^* &= \frac{p_n + p_{n-1}}{2} + \Delta t F_p(v_n, p_n) \end{aligned} \tag{10}$$

Corrector:

$$\begin{aligned} (I - G)(v_{n+1} - v_n) &= \Delta t F_v(v_n, b^*, p^*) \\ b_{n+1} - b_n &= \Delta t F_b\left(\frac{v_n + v_{n+1}}{2}, b^*\right) \\ p_{n+1} - p_n &= \Delta t F_p\left(\frac{v_n + v_{n+1}}{2}, p^*\right) \end{aligned} \tag{11}$$

The subscript i indicates the time step. v_i, b_i and p_i are the velocity, the magnetic and the pressure fields, respectively, and F_b, F_p and F_v the nonlinear ideal MHD right-hand sides of Faraday's equation, pressure evolution equation and equation of motion, respectively. Here, the pressure evolution in Eq. (2) is used. If ρ and T are advanced in time according to Eq. (3), the predictor and corrector step on p in Eqs. (10) and (11) is replaced by predictor and corrector steps on ρ and T.

Contrary to a leapfrog time step, the multi-step predictor step on B and p is no more reversible and acts to damp all the fast waves (see Fig. 1, where $|\lambda|$ is always less than 1). This reduces strongly the noise as, e.g. can be observed in Fig. 3 at the beginning of the simulation.

The numerical stabilizing operator is $G = \alpha L_0 \Delta t^2 + c\nabla^2$, where L_0 is the linearized ideal second-order full MHD operator. α and c are parameters introduced for the purpose of the stability study of the scheme. The effects of α and c in G on the linear and nonlinear stability of the scheme are described in Sections 3.3 and 3.4, respectively.

- α only acts on the linear numerical stability, and does not affect the low frequency Alfvén modes targeted with XTOR.

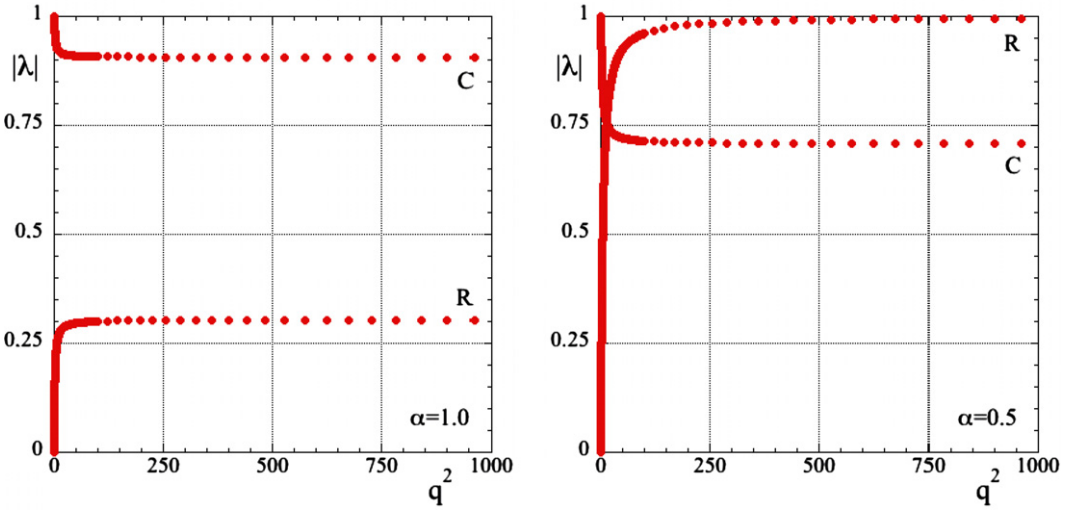

Fig. 1. Moduli of the roots of Eq. (15) for $\alpha = 1.0$ and $\alpha = 0.5$.

- c only acts on the nonlinear stability but does not exactly respect the structures of the low frequency Alfvén modes. c must therefore be kept small, typically several Δr^2, where Δr is the radial mesh size.

3.3. Linear stability

First, let us consider the linear numerical stability of this time advance scheme. For the linear stability study, we suppose that $c = 0$ in $I - G$. The time advance is then diagonal for MHD modes and it can be computed independently for each MHD eigenvector and eigenmode. Let ω^2 be an eigenvalue of $-L_0$ and V and B the velocity and magnetic field in the corresponding eigenspace (pressure which behaves as B is omitted for simplicity),

$$\begin{cases} \dot{V} = L_v B \\ \dot{B} = L_b V \\ \ddot{V} = -\omega^2 V \end{cases} \tag{12}$$

L_v and L_b are the linear right-hand sides of the ideal MHD equation of motion and Faraday's equation, respectively. Note that $L_0 = L_v L_b$. Denoting v and b the complex amplitude of V and B in this eigenspace and setting $q = \omega \Delta t$, Eq. (12) can easily be mapped into

$$\begin{cases} \dot{v} = iqb \\ \dot{b} = iqv. \end{cases} \tag{13}$$

For each eigenspace, the physical (linear) equations are given by Eq. (13). Applying this to the semi-implicit algorithm defined by Eqs. (10) and (11) and noting that $I - G = 1 + \alpha q^2$ the following recursive set of equations is obtained:

$$\begin{aligned} v_{n+1} &= \left(1 - \frac{q^2}{1+\alpha q^2}\right) v_n + \frac{iq}{1+\alpha q^2}\left(\frac{b_n + b_{n-1}}{2}\right) \\ b_{n+1} &= \frac{iq}{2}\left(2 - \frac{q^2}{1+\alpha q^2}\right) v_n + \left(1 - \frac{q^2}{4(1+\alpha q^2)}\right) b_n - \frac{q^2}{4(1+\alpha q^2)} b_{n-1} \end{aligned} \tag{14}$$

The characteristic equation of this system reads

$$4\lambda(\lambda-1)[(1+\alpha q^2)\lambda+(1-\alpha)q^2-1]+q^2(\lambda+1)^2=0 \tag{15}$$

The time advance scheme is linearly stable if the modulus of the roots λ of Eq. (15) are less than 1 for every q and a given value of α. Except for the special case $q=0$, Eq. (15) has one real and two complex conjugate roots. In Fig. 1, their moduli are presented for $\alpha=1.0$ and $\alpha=0.5$. R and C indicate the real and the complex roots, respectively. Fig. 1 shows that the case $\alpha=1.0$ is unconditionally stable linearly, whereas the case $\alpha=0.5$ is marginally stable because for $q^2\to\infty$, $|\lambda_R|\to 1$. For $\alpha<0.5$, the time advance scheme becomes linearly unstable. XTOR runs with $\alpha=1$ because of nonlinear stability issues discussed in Section 3.4.

3.4. Nonlinear stability

Second, let us consider the nonlinear numerical stability of the time advance scheme. In this regime, the time advance scheme is limited by conditions on the velocity, the non-axisymmetric magnetic field and the departure of the axisymmetric background from the initial one.

The velocity convection is treated explicitly in XTOR. Therefore the time step is constrained by a CFL condition on the velocity. The most stringent condition on the time step Δt arises at the poloidal mesh center with

$$m_{\max}\|\mathbf{v}\|\Delta t<\Delta r \tag{16}$$

where $\|\mathbf{v}\|$ is the norm of the velocity, $m_{\max}$ is the maximum poloidal mode number in the simulation and Δr is the radial mesh size.

With $G=\alpha L_0\Delta t^2$ the time advance scheme would be unstable in the nonlinear phase because of the explicit treatment of the nonlinear departure of the magnetic field dynamics from the linear one. The main effect is due to modifications of the Alfvén spectrum associated to the nonlinear radial magnetic field which is orthogonal to the equilibrium magnetic field. A numerical instability would grow near the axis as soon as

$$m_{\max}\delta B\Delta t/\Delta r>1. \tag{17}$$

where δB is the radial component of the magnetic field. As in Ref. [18] the stabilizing semi-implicit operator is completed by a Laplacian contribution $G=\alpha L_0\Delta t^2+c\nabla^2$ to relax the time step limitation (17). The parameter c has no dissipation effect on the mode dynamics. However, it must be kept small in order to reduce its dispersion effect on the dynamics of the instability in the vicinity of its resonant layer (typically a few Δr^2). The time step in the nonlinear phase of the simulation then is limited by the condition,

$$c\geqslant\frac{c}{k_1^2}\geqslant(\Delta t\delta B)^2. \tag{18}$$

In XTOR, k_1 is a numerical factor set to 1.2 in order to keep a margin with respect to the stability condition (18). With standard run parameters, e.g. $\Delta r=5.10^{-3}$, $m=32$, $c=5\times10^{-4}$, Eq. (18) allows a $\approx$150 times larger time step than Eq. (17) applied at the mesh axis. In the nonlinear phase of an XTOR simulation, the time step is usually limited by Eq. (18). Eq. (16) only controls the time step in rare occasions such as the saturation of an ideal MHD internal $m/n=1/1$ kink instability with a large growth rate. Typical time steps in a XTOR simulation with the above standard run parameters are $\Delta t=10\tau_a$ in the linear phase. In the nonlinear phase Δt drops to a few $10^{-2}\tau_a$ for an instability which moves the plasma core away from the discretization mesh center (e.g. an internal kink), and $\Delta t\approx 1$ to $3\tau_a$ for instabilities with dynamics away from the poloidal mesh center (e.g. tearing or ballooning instabilities).

The $I-G$ operator is computed for the first time using the initial equilibrium. As the plasma profiles evolve, the semi-implicit stabilization operator has to be recomputed from time to time, and we succeeded in the derivation of a criterion which triggers this operation. Coming back to Eqs. (14) and (15) it can be checked that the stability is ensured for a given mode if $q^2/(1+\alpha q^2)<2$. For an arbitrary increment δv, this relation becomes using the relations (12), $L_0=L_vL_b$, $q^2\delta v=-\Delta t^2L_0\delta v$ and $(1+\alpha q^2)\delta v=(I-G)\delta v$

$$\frac{\langle(I-G)^{-1}\Delta t^2L_0\delta v^i|\delta v_j\rangle}{\langle\delta v^i|\delta v_j\rangle}<2 \tag{19}$$

In Eq. (19), the bracket $\langle\cdots\rangle$ is the scalar product for which L_0 and G are self-adjoint.

In XTOR, $\alpha = 1$ is used and therefore the LHS of Eq. (19) is bounded by 1 (bounded by 2 for $\alpha = 1/2$ which is the stability limit in Fig. 1). This provides a security factor for the nonlinear stability which is used as follows. Eq. (19) can be seen as a linear stability criterion when due to the evolution of the plasma profiles, the linear MHD operator (L_0) evolves whereas G remains unchanged (because $I - G$ has been decomposed and stored). Therefore, every few time steps (typically 5) $L_t\delta v^i$ is computed, where δv^i is the current velocity increment and L_t the second-order MHD operator obtained with $n = 0$ projections of the magnetic and pressure fields at time t. Then

$$\frac{\langle (I-G)^{-1}\Delta t^2 L_t \delta v^i | \delta v_j\rangle}{\langle \delta v^i | \delta v_j\rangle} \leqslant k_2 < 2 \tag{20}$$

is imposed. k_2 is a margin and is generally set to 1.2 in XTOR. If Eq. (20) is violated, $(I - G)^{-1}$ is replaced by $(1 - \alpha\Delta t^2 L_t - c\nabla^2)^{-1}$ (which requires another LU decomposition). In long time simulations (for example the tearing dynamics over several $10^5\tau_a$) typically 2 or 3 of such matrix decompositions occur.

As usual in nonlinear stability problems, it is difficult to derive rigorously the stability criteria. Nevertheless it was observed in all the simulations done with XTOR that it has always been sufficient to fulfill the criteria (16), (17), (20) to ensure numerical stability.

3.5. Time advance method of the non-ideal MHD part

XTOR uses a split time advance [1] which separates the advance of the ideal MHD, the magnetic diffusion and the thermal diffusion parts of the equations. The advantages of such a method are first, that the physical properties such as self-adjointness of the ideal MHD and transport operators are easily preserved when the problem is discretized. Such properties are much more difficult to preserve with an operator including non-ideal MHD terms and the same discretization as XTOR. Second, different numerical methods can be used for the time advance of the different parts of the equations.

In the present version of XTOR, the resistive part of Faraday's equation is advanced semi-implicitly. The numerical stabilizing matrix is constructed and inverted once per simulation by discretizing $1 - \Delta t_0 \nabla \times \eta_0 \times \nabla\times$. η_0 is the equilibrium resistivity profile and Δt_0 the initial time step. During the simulation both η and Δt vary. Thus the time step must satisfy

$$\eta_0 \Delta t_0 \geqslant \eta \Delta t \tag{21}$$

everywhere in the plasma for numerical stability. This condition is rarely violated.

The thermal diffusion part of the equations is advanced fully implicitly by a preconditioned conjugate gradient method. This sub-step is unconditionally stable numerically. The computational efficiency of this method is a direct consequence of the quality of the pre-conditioner. Here, it is obtained from the inverse of $1 - \Delta t_0(\nabla\chi_\perp\nabla + \nabla\cdot[\mathbf{B_0}\chi_\parallel/B_0^2(\mathbf{B_0}\cdot\nabla)])$. Depending on the value of $\chi_\perp$, either the entire LU decomposition is conserved for preconditioning (the matrix stored in Fourier space is block tri-diagonal in this case), or only the diagonal blocks or only the diagonal elements are conserved. The pre-conditioner is reevaluated if the current time step differs by a factor larger than 3 or smaller than 1/3 from Δt_0. With these rules the conjugate gradient method converges in about 1–3 iterations per time step in the linear phase of the simulation. In the nonlinear phase the number of iterations increases to typically 40–80. Indeed the preconditioning worsens because of the departure of the magnetic field from the equilibrium one, in particular in regions where the magnetic field becomes stochastic.

3.6. Initial conditions and discretization method

3.6.1. Equilibrium input quantities

XTOR uses finite differences in the radial and Fast Fourier Transforms (FFT) in the poloidal and the toroidal directions. The angular mesh in the poloidal plane is the polar angle θ. The angle in the toroidal direction is the toroidal angle Φ. Both angular discretization meshes are equiangular. Radially, the code uses two staggered magnetic flux coordinate meshes labeled (r_l) and $(r_{l+1/2})$ with

$$r = \sqrt{(\Psi/\Psi_{\mathrm{surf}})}. \tag{22}$$

where Ψ is the equilibrium poloidal magnetic flux and Ψ_{surf} its value at the plasma surface. If the equilibrium does not change significantly during the simulation this choice reduces somewhat the required poloidal mesh resolution. Indeed the resonant surfaces of the instabilities coincide with the equilibrium poloidal flux surfaces.

The radial mesh in XTOR is obtained from the solution of the Grad-Shafranov equation,

$$\nabla \cdot \frac{1}{R^2}\nabla\Psi = \frac{j_\phi}{R} = -p'(\Psi) - \frac{1}{R^2}FF'(\Psi) \tag{23}$$

solved here by the CHEASE code [21,22]. In Eq. (23), p is the equilibrium plasma pressure, F is the equilibrium toroidal magnetic flux function and j_Φ is the toroidal equilibrium current density. R is the major radius in the torus. Using a polar mesh θ in the poloidal direction in XTOR has the advantage that the metrics computed by the CHEASE code do not depend on the second derivative of the equilibrium solution Ψ, contrary to the ones of, e.g. a straight field line coordinate system [22]. This increases significantly their accuracy.

Note that as the (r,θ) mesh is non-diagonal in the poloidal plane the corresponding non-diagonal metric terms are non-zero, which increases somewhat the amount of algebra in the operators. The metric elements are an important output of CHEASE because they are used to construct all the operators in XTOR.

This metric was already described in Ref. [22]. The contra-variant metric is $(g^{ij}) = (g_{ij})^{-1}$. $D = [\nabla r, \nabla\theta, \nabla\phi]$ is the reciprocal of the Jacobian, $\|g^{ij}\| = D^2$. The metric elements are needed on the (r_l,θ_k) and $(r_{l+1/2},\theta_k)$ meshes. Moreover, CHEASE provides XTOR with equilibrium profiles which are evaluated on the (r_l) and $(r_{l+1/2})$ meshes. All the equilibrium quantities required as input by XTOR are summarized in Table 1.

3.6.2. Field discretizations

In XTOR, the derivatives in the angular direction are evaluated by Fourier transforms. Therefore, they are local in space. Radially, the derivatives require a staggered mesh, i.e. the derivative of a quantity discretized on the integer mesh (r_l) is evaluated on the half-integer mesh $(r_{l+1/2})$, and vice versa.

The choice was made to evaluate scalar fields, i.e. p, ρ, T, velocity and magnetic field divergence, on the half-integer mesh $(r_{l+1/2})$. Because of the finite differences used in the radial direction, the radial components of the velocity and the magnetic field are evaluated at the integer mesh (r_l), whereas their angular components are evaluated at the half-integer mesh. $\mathbf{E} = \mathbf{v}\times\mathbf{B}$ and $\mathbf{J} = \nabla\times\mathbf{B}$ are discretized on the half-integer mesh $(r_{l+1/2})$ and the integer mesh (r_l) for the radial and the angular components, respectively. For every vector field, the co- or contra-variant components are discretized with the same radial mesh. The contra-variant θ component of the fields are singular at the poloidal mesh axis, they behave $\propto 1/r$. To avoid this singularity, $v^\theta/D, B^\theta/D, J^\theta/D$ is used as a variable (close to the mesh axis, $D\propto 1/r$). By symmetry, $v_\theta D, B_\theta D, J_\theta D$ are used in the covariant representation (the covariant θ components of the fields are $\propto r$ in the vicinity of the mesh axis). The localizations of the discretized variables used in XTOR are summarized in Table 2. Its left column shows the fields in use, whereas its right column shows the mesh nodes where these quantities are evaluated in

Table 1
Initial equilibrium quantities

	CHEASE equilibrium quantities for XTOR
1	$D = \frac{1}{R}\left(\frac{\partial r}{\partial R}\frac{\partial\theta}{\partial Z} - \frac{\partial r}{\partial Z}\frac{\partial\theta}{\partial R}\right)$
2	$g^{rr} = \left(\frac{\partial r}{\partial R}\right)^2 + \left(\frac{\partial r}{\partial Z}\right)^2$
3	$g^{r\theta} = \frac{\partial r}{\partial R}\frac{\partial\theta}{\partial R} + \frac{\partial r}{\partial Z}\frac{\partial\theta}{\partial Z}$
4	$g^{\theta\theta} = \left(\frac{\partial\theta}{\partial R}\right)^2 + \left(\frac{\partial\theta}{\partial Z}\right)^2$
5	$g^{\Phi\Phi} = \frac{1}{R^2}$
6	$p(r)$
7	$p'(r)$
8	$F(r)$
9	$FF'(r)$
9	$\mathbf{J}_{\mathrm{boot},\mathbf{0}}(r)$
10	$\frac{\mathrm{d}r}{\mathrm{d}\Psi}$

XTOR. The same rules as in Section 3.6.1 apply, i.e. (r_l) and $(r_{l+1/2})$ denote the radial integer and half-integer discretization mesh, respectively. (θ_k) indicates the integer poloidal mesh.

The representation used for the velocity and the magnetic field is contra-variant in the ideal MHD part of Eqs. (1)–(3). The RHS of the equation of motion is naturally covariant. But the application of $(I-G)^{-1}$ modifies the representation from co- to contra-variant, i.e.

$$\begin{aligned}
\partial_t \mathbf{v}^{\mathbf{i}} &= [(I-G)^{-1}\{-(\mathbf{v}^{\mathbf{k}}\cdot\nabla)\mathbf{v}^{\mathbf{k}} + \mathbf{J}^{\mathbf{k}}\times\mathbf{B}^{\mathbf{k}} - \nabla p + \nabla v \nabla \mathbf{v}^{\mathbf{k}}\}_j]^i \\
\partial_t \mathbf{B}^{\mathbf{i}} &= (\nabla\times(\mathbf{v}^{\mathbf{k}}\times\mathbf{B}^{\mathbf{k}})_j)^i \\
\partial_t p &= -\Gamma p \nabla\mathbf{v}^{\mathbf{i}} - \mathbf{v}^{\mathbf{i}}\cdot(\nabla p)_i
\end{aligned} \tag{24}$$

Symbolically, we kept the notation $I-G$ but the identity is in fact g_{ij} in order to switch from co- to contra-variant representation.

3.6.3. Mode filtering

The algebra in the poloidal plane involves non-orthogonal metrics, which are provided by the CHEASE code [21,22]. The poloidal mode structure of the metric terms for equilibria with a non-circular poloidal cross-section is relatively broad. Therefore, algebraical operations must be followed by frequent projections on the poloidal mode set used by XTOR. Of course these projections have to respect the properties of the operators involved in the XTOR model, such as the self-adjointness. As an example, using the same notations as in Ref. [33, Chapter 7, p. 126] for the algebra, and applying this to the ideal part of Faraday's equation reads with cyclic permutations

$$\begin{aligned}
E_k &= \prod_{m,n}(v^i B^j - v^j B^i)/D \\
\partial_t B^k &= \prod_{m,n} D\left(\frac{\partial E_i}{\partial\theta^j} - \frac{\partial E_j}{\partial\theta^i}\right)
\end{aligned} \tag{25}$$

where $(\theta^1,\theta^2,\theta^3) = (r,\theta,\phi)$ is the curvilinear coordinate system used in XTOR and $\prod_{m,n}$ is the projector on the (m,n) mode set used by XTOR in the simulation. In order to keep the ideal second-order MHD operator self-adjoint, the Laplace force contribution to the equation of motion reads

$$\begin{aligned}
B_i &= \prod_{m,n} g_{ij} B^j \\
J^k &= \prod_{m,n} D\left(\frac{\partial B_i}{\partial\theta^j} - \frac{\partial B_j}{\partial\theta^i}\right) \\
\partial_t v_k^{Laplace} &= \prod_{m,n}(J^i B^j - J^j B^i)/D
\end{aligned} \tag{26}$$

Table 2
Field discretizations

	XTOR field	XTOR mesh node
1	$v_r,\ v^r$	$(r_l,\ \theta_k)$
2	$Dv_\theta,\ v^\theta/D$	$(r_{l+1/2},\ \theta_k)$
3	$v_\Phi,\ v^\Phi$	$(r_{l+1/2},\ \theta_k)$
4	$B_r,\ B^r$	$(r_l,\ \theta_k)$
5	$DB_\theta,\ B^\theta/D$	$(r_{l+1/2},\ \theta_k)$
6	$B_\Phi,\ B^\Phi$	$(r_{l+1/2},\ \theta_k)$
7	$J_r,\ J^r$	$(r_{l+1/2},\ \theta_k)$
8	$DJ_\theta,\ J^\theta/D$	$(r_l,\ \theta_k)$
9	$J_\Phi,\ J^\Phi$	$(r_l,\ \theta_k)$
10	$p,\ T,\ \rho$	$(r_{l+1/2},\ \theta_k)$
11	η	$(r_l,\ \theta_k)$

Similar rules must be applied to the other contributions, both for the ideal and the non-ideal MHD terms.

The projector $\prod_{m,n}$ also acts as des-aliasing in the poloidal and toroidal directions. For that purpose the toroidal and poloidal resolutions of the fields are chosen to be at least $3/2$ times larger in the Fourier space than the modes actually advanced in time in a simulation [34].

3.7. Boundary conditions

Much care is necessary in handling the boundary conditions, especially at the mesh center. XTOR solves the extended MHD equations with a perfectly conducting shell at the plasma surface. The plasma surface therefore is a magnetic flux surface. The boundary conditions on the different fields evolving in XTOR are imposed consistently with the physics solved in every sub-step of the time advance scheme.

First, consider the time advance of the ideal MHD sub-step. Free slip conditions are imposed on the velocity field, i.e.

$$v_p^r = 0; \quad \partial_r v_p^\theta = 0; \quad \partial_r v_p^\Phi = 0 \tag{27}$$

The subscript p indicates the plasma boundary. Since the angular components of the velocity and of the increments of the magnetic and the pressure fields are defined on the half-integer mesh, a ghost point is used half a discretization interval outside the plasma to impose the conditions (27).

For the initial magnetic and pressure field, the conditions at the plasma boundary are obtained from the CHEASE code [21,22]. The equilibrium magnetic field satisfies $B_{eq}^r = 0$ everywhere. Therefore, since $v_p^r = 0$ from Eq. (27), no boundary conditions are required at the plasma boundary on the ideal MHD increments of the magnetic field and the pressure (or the temperature and the density). Indeed, with $v_p^r = B_p^r = 0$ with the staggered mesh representation as described in Section 3.6.2, E_θ and E_Φ which are defined on the integer mesh vanish at the plasma boundary for the ideal MHD part of the equations.

Second, the time increment of the resistive part of Faraday's equation requires a plasma boundary condition on the angular current density components J_p^Φ and J_p^θ at the plasma surface. J_p^θ is constrained by $\partial_r \delta B_{p\Phi} = \partial_r g_{\phi\phi,p} \delta B_p^\Phi = 0$ at the plasma boundary, and $J_{\Phi,p}$ by demanding that

$$E_{\Phi,0,p} = \eta_0 J_{\Phi,p,0} = \eta_p(t) J_{\Phi,p}(t) = \eta_p(t) g_{\phi\phi} J_p^\Phi(t) = E_{//} \tag{28}$$

throughout the simulation, where $E_{//}$ is a real constant which represents the loop voltage.

At the center of the poloidal mesh, the boundary conditions are imposed using a method which has proved its robustness in the CHEASE code [21,22]. For the velocity and the magnetic field, the radial component defined on the integer mesh is required at the axis. As an example for the contra-variant velocity field, it is obtained by evaluating at the first half-integer mesh node the averages

$$\begin{aligned} \sum_{i=0}^{m_{\max}-1} \frac{v_i^\theta}{\sqrt{g_i^{\theta\theta}}} \cos(\theta_i) &= -v_R \sum_{i=0}^{m_{\max}-1} \sin(\theta_i)\cos(\theta_i) + v_Z \sum_{i=0}^{m_{\max}-1} \cos^2(\theta_i) \\ \sum_{i=0}^{m_{\max}-1} \frac{v^{\theta_i}}{\sqrt{g_i^{\theta\theta}}} \sin(\theta_i) &= -v_R \sum_{i=0}^{m_{\max}-1} \sin^2(\theta_i) + v_Z \sum_{i=0}^{m_{\max}-1} \sin(\theta_i)\cos(\theta_i) \end{aligned} \tag{29}$$

The $\theta_i,\ i = 0, \ldots, m_{\max} - 1$ denote the poloidal angles in the physical space. Solving this system gives (v_R, v_Z), which is used to evaluate v^r at the mesh center with

$$v_i^r = \sqrt{g_i^{rr}} (v_R \sin(\theta_i + \omega_i) - v_Z \cos(\theta_i + \omega_i)) \tag{30}$$

for $i = 0, \ldots, m_{\max} - 1$ and

$$\omega_i = \arccos\left(\frac{g_{r\theta}^i}{g_{rr}^i g_{\theta\theta}^i}\right) = \arccos\left(-\frac{g_i^{r\theta}}{g_i^{rr} g_i^{\theta\theta}}\right). \tag{31}$$

Similarly for the covariant velocity field, the solution at the first half-integer mesh node of

$$\begin{aligned}\sum_{i=0}^{m_{\max}-1}\frac{v_\theta^i}{\sqrt{g_{\theta\theta}^i}}\cos(\theta_i) &= v_R\sum_{i=0}^{m_{\max}-1}\cos(\theta_i+\omega_i)\cos(\theta_i)+v_Z\sum_{i=0}^{m_{\max}-1}\sin(\theta_i+\omega_i)\cos(\theta_i)\\ \sum_{i=0}^{m_{\max}-1}\frac{v_\theta^i}{\sqrt{g_{\theta\theta}^i}}\sin(\theta_i) &= v_R\sum_{i=0}^{m_{\max}-1}\cos(\theta_i+\omega_i)\sin(\theta_i)+v_Z\sum_{i=0}^{m_{\max}-1}\sin(\theta_i+\omega_i)\sin(\theta_i)\end{aligned} \tag{32}$$

is injected into

$$v_r^i=\sqrt{g_{rr}^i}(v_R\cos(\theta_i)+v_Z\sin(\theta_i)) \tag{33}$$

to evaluate the covariant radial velocity component at the poloidal mesh center. B^r and B_r are obtained in the same manner at the mesh axis. Furthermore, one ghost point is used left of the half-integer mesh center for every angular component of the fields. There the values of the fields are obtained by symmetry conditions and used to evaluate radial derivatives at the mesh center. Again as an example, for the contra-variant velocity field

$$\begin{aligned}v^\theta(-h/2) &= (-1)^{m+1}v^\theta(h/2)\\ v^\Phi(-h/2) &= (-1)^m v^\Phi(h/2)\end{aligned} \tag{34}$$

where h is the radial mesh size and $m=0,\ldots,m_{\max}-1$ the poloidal mode number. These symmetry conditions are also imposed at the same locations on $v_\theta, B^\theta, B_\theta$ and $v_\Phi, B^\Phi, B_\Phi, p, \rho, T$ which behave like v^θ and v^Φ, respectively. All the boundary conditions on the fields are evaluated in the physical space at every toroidal mesh node $\Phi_k, k=0,\ldots,n_{\max}-1$.

Boundary conditions are also required for the current density and the induction at the mesh center. The radial components of these fields are defined on the half-integer mesh and the angular components on the integer mesh. Thus the radial co- and contra-variant components of both fields satisfy the same symmetry conditions as the polar components of the velocity and magnetic fields at the mesh center, Eq. (34). The angular components of the induction and the current density, both defined on the integer mesh, are required at the mesh axis. Only the covariant components of the induction are required, and directly evaluated from the vector product of velocity with magnetic field. The situation is different for the angular components of the current density, where Ampère's law is applied at the first half-integer mesh node to give

$$J^\Phi(r=0)=\frac{4}{h}\frac{\sum_{i=0}^{m_{\max}-1}B_\theta^i}{\sum_{i=0}^{m_{\max}-1}R_iD_i}. \tag{35}$$

Using this set of prescription the behavior near the mesh center was found to be satisfactory in all the simulations done with XTOR.

At moment, the study of external modes in real tokamak geometry is limited with XTOR because it is supposed that an infinitely conducting wall is located at the plasma surface. A vacuum between the plasma surface and the wall can be simulated by a current free and high resistivity plasma as long as no equilibrium separatrix is located in that region. A full solution of this problem would require the possibility of handling a plasma equilibrium separatrix and piloting the plasma equilibrium with a system of poloidal coils.

3.8. Linear algebra

The matrices used in XTOR are defined in the Fourier space. The matrices are diagonal in n due to the symmetry of the background equilibrium. The linear ideal MHD operator is bloc-pentadiagonal and is inverted using a standard bloc-LU decomposition. This procedure is widely employed in codes using Fourier expansions in the angular directions and will not be recalled here. Nevertheless, two points are emphasized.

First, the projectors $\prod_{m,n}$ defined in Section 3.6.3 select modes which are necessary for a given evolution. This restricts the size of the blocs in the matrices and allows LU decompositions even for a large resolution. For example, certain studies in [29,30] were done using 128 poloidal grid points but with a projection on 48 modes only. The most difficult cases arise for evolutions with a strong ballooning component.

Secondly, the matrix constructions has to be done automatically. A direct writing of the matrix elements is difficult because of the mixing of operations in the real and the Fourier space due to the projectors $\prod_{m,n}$ in Eqs. (25) and (26). Thus for the construction of the matrices the linear operators are applied successively on basis functions. Basically, for the construction of the linear ideal MHD stability matrix L_0 is applied on each velocity component, each Fourier mode at each grid point. But as L_0 is bloc-pentadiagonal, this can be done at the same time on grid points separated by five radial mesh intervals. Moreover, if boundary conditions are correctly applied to the basis vectors it ensures that they are automatically taken into account in the linear algebra.

4. Applications

4.1. Internal kink mode cycling

The first test case shows the cycling of a toroidal $m/n = 1/1$ internal kink in time. The internal kink is connected with the so-called sawtooth oscillations in tokamak plasmas, a periodic and sudden relaxation of the

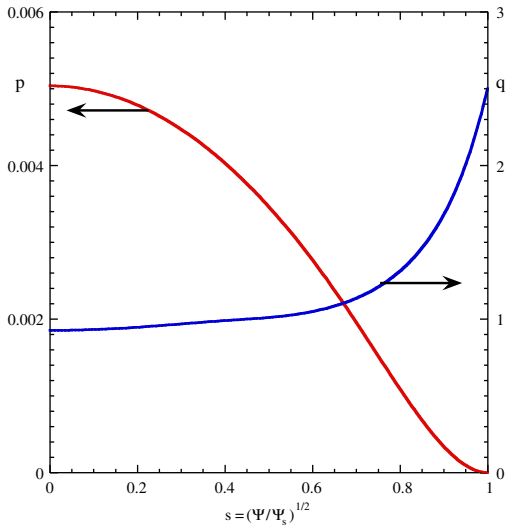

Fig. 2. Initial equilibrium profiles for the internal kink mode simulation.

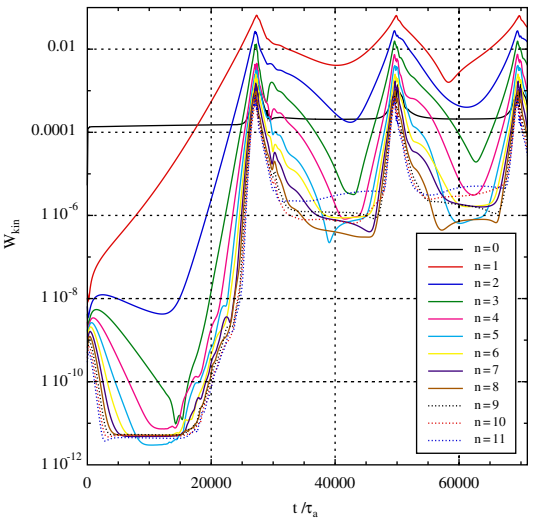

Fig. 3. Time evolution of kinetic energy of toroidal modes.

core plasma temperature inside the $q = m/n = 1$ radius. The case presented in Fig. 3 starts with a low poloidal beta equilibrium ($\beta_p = 0.16$) which is linearly ideal MHD stable but resistive MHD unstable. The initial equilibrium has a circular poloidal cross-section with an aspect ratio of 2.7. Its pressure and q-profile are shown in Fig. 2.

The model used in XTOR for this simulation is resistive MHD with thermal transport. The transport source is chosen to be $H = -\nabla\chi_\perp\nabla p_0$, i.e. to rebuild the equilibrium pressure profile p_0 after a perpendicular transport characteristic time. The cyclic behavior is obtained by setting the perpendicular transport coefficient $\chi_\perp$ to a significantly larger value than the resistivity η. Here, $\eta = 10^{-6}$ at the magnetic axis and $\chi_\perp = 3 \times 10^{-4}$ throughout the plasma. This ensures that the core equilibrium pressure (i.e. the finite pressure threshold of the toroidal internal kink [4]) is rebuilt on a faster time scale than the growth of the internal kink. With a smaller value of $\chi_\perp$ (say $\chi_\perp = \eta$) the plasma stabilizes itself after a few cycles in a stationary state where $q = 1$ everywhere in the plasma core and the central equilibrium pressure never recovers. Note that it is unclear if after a

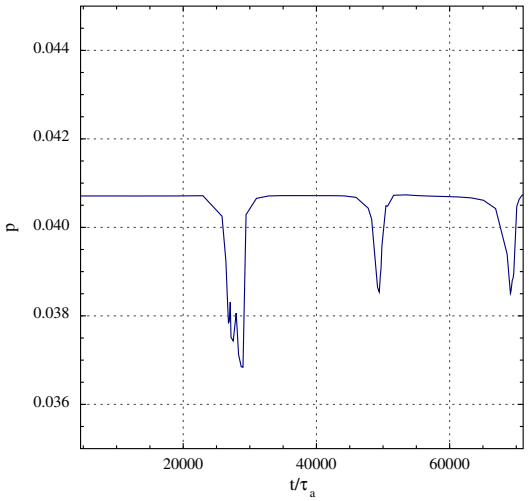

Fig. 4. Time evolution of central pressure.

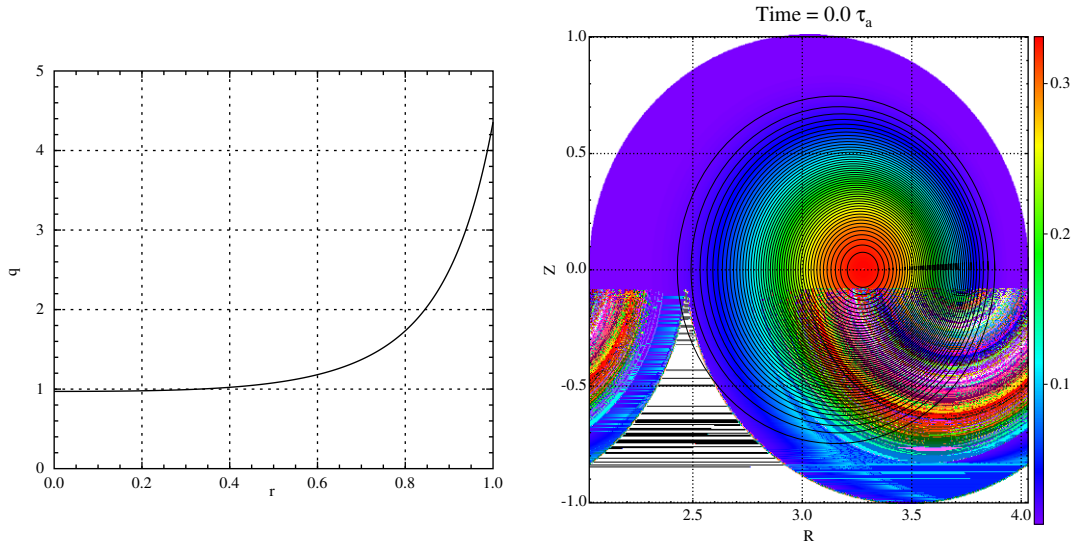

Fig. 5. Equilibrium q-profile and pressure contours used in the kink-ballooning simulations.

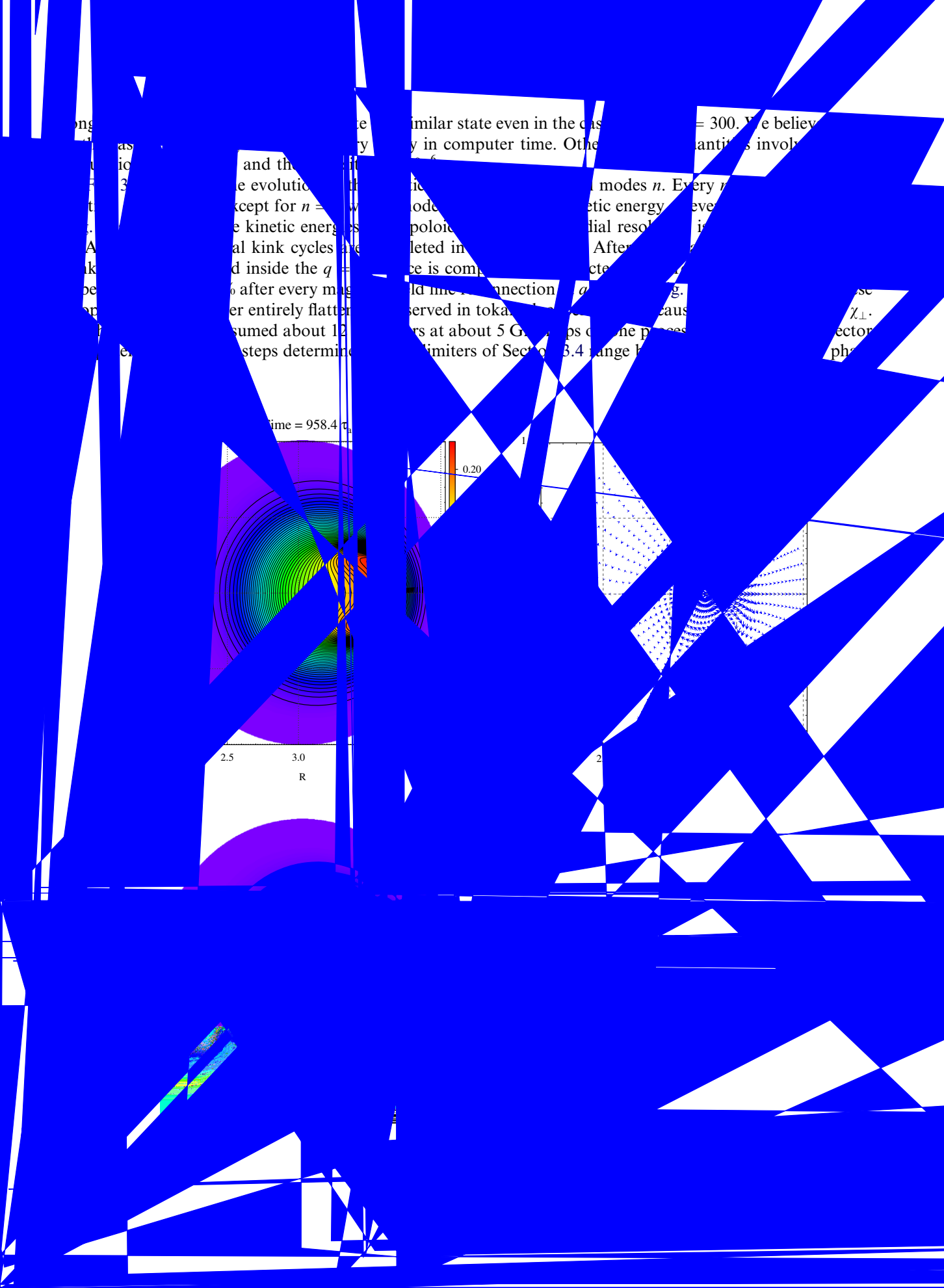
0.20
2.5
3.0
R

and $3 \times 10^{-2}\tau_a$ in the most nonlinear phase corresponding to the middle of the magnetic reconnection phase. The main limitation comes from v^θ at the mesh axis.

4.2. Moderate-n ballooning mode destabilizations by internal kinks

The nonlinear destabilization of moderate-n ballooning modes first was observed and simulated in the TFTR tokamak [35]. A parameter study has shown that in ideal MHD, it occurs above a finite pressure threshold [23]. It was also shown that this threshold significantly drops with poloidal plasma cross-section shaping and plasma resistivity [36].

Here, two test cases are presented. The initial equilibria differ only by a scaling factor in the pressure profile. A contour plot of the equilibrium pressure and q-profile are shown in Fig. 5. The poloidal plasma cross-section

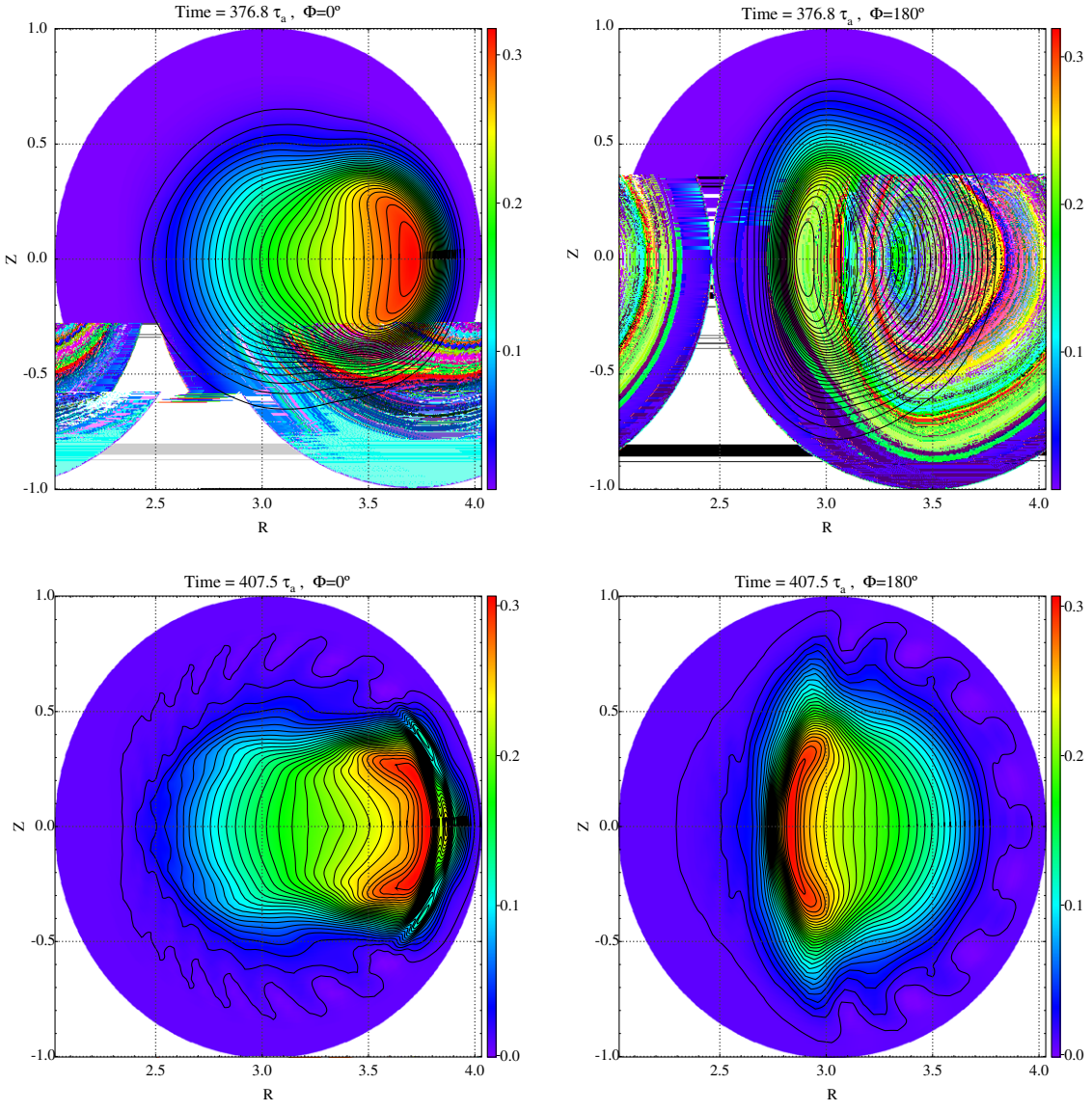

Fig. 7. Pressure contours of kink-ballooning evolutions in resistive MHD with transport at $\Phi = 0^\circ$ (left) and $\Phi = 180^\circ$ (right).

is circular and the aspect ratio of the torus $A = 3$. The $q = 1$ radius is $r_{q=1} = (\Psi_{q=1}/\Psi_s)^{1/2} = 0.33$ and the magnetic shear at $q = 1$ is $s_{q=1} = 0.08$.

The first simulation is an ideal MHD simulation with the same initial equilibrium as in Ref. [23]. The poloidal beta of the initial equilibrium is $\beta_p = 1.08$. The time evolution of the pressure contours and the velocity flow patterns at $\Phi = 0^\circ$ are shown in Fig. 6 at $t = 958$ and $1083\tau_a$, where τ_a is the toroidal Alfvén time. At $t = 958\tau_a$ only the internal kink pressure deformation is observed, steepening the pressure profile at the low magnetic field side of the torus. Later at $t = 1083\tau_a$, moderate-n ballooning modes are destabilized nonlinearly (the most unstable ballooning mode has $m = 8$ and $n = 8$). They create bulges which are more pronounced at the low than the high magnetic field side of the isobars (which is characteristic for ballooning instabilities) and which develop in time into finger-like structures. The corresponding convection cells can be observed on the velocity flow patterns. Note that at $\theta = 0^\circ$ the internal kink bounces back. This is frequently observed in high β ideal MHD internal kink simulations.

The second simulation uses the same initial equilibrium profiles as the preceding one except for a scaling factor in the pressure giving $\beta_p = 1.75$. Furthermore this simulation was done including resistivity and transport. The moderate n ballooning modes are linearly stabilized by thermal transport and a higher β_p than in the ideal MHD case is required to destabilize them nonlinearly by the internal kink. $\eta = 10^{-6}$ in the plasma center and $\chi_{//}$ and $\chi_\perp$ are set to 10 and 10^{-6}, respectively. The evolution of the isobars at $\Phi = 0^\circ$ and $\Phi = 180^\circ$ are shown in Fig. 7 at $t = 377$ and $407\tau_a$. Due to the resistivity, the dynamics of the internal kink is much faster. It can be observed that during the saturation process for a resistive internal kink with such a high growth rate, the pressure diffuses through the $q = 1$ surface and is blocked farther outside against another rational surface (here $q = 2$). This diffusion has a strong ballooning component since the pressure perturbation is blocked by the high magnetic field as seen in Fig. 7 with $\Phi = 180^\circ$.

Both simulations were done with 200 radial points, 11 toroidal modes (including $n = 0$). Every toroidal mode has a resolution of 24 poloidal modes. These simulations costed 2 and 4 hours cpu time at about 5 Gigaflops on one processor of a NEC SX8 vector computer for the ideal and the non ideal MHD cases, respectively.

4.3. Nonlinear destabilization of a Neoclassical Tearing Mode

Neoclassical Tearing Modes (NTM's) have been observed in most of todays tokamak experiments since their discovery in TFTR [37]. These instabilities are linearly stable, and require a finite magnetic seed at their resonant surface to be destabilized. Good candidates for providing these seeds are the internal kink instability

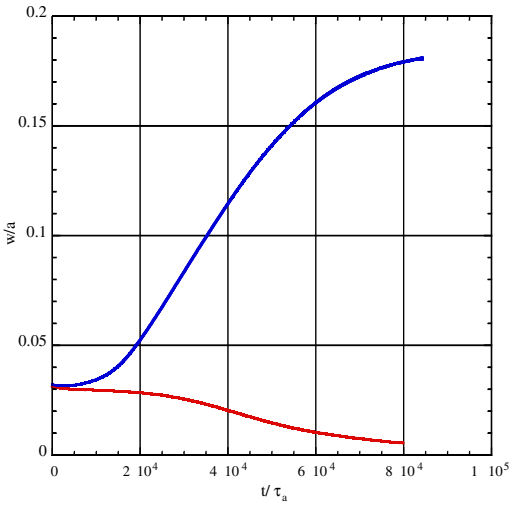

Fig. 8. Time evolution of a $m/n = 3/2$ NTM island size about its nonlinear stability threshold at $w_-/a \approx 3.1\%$.

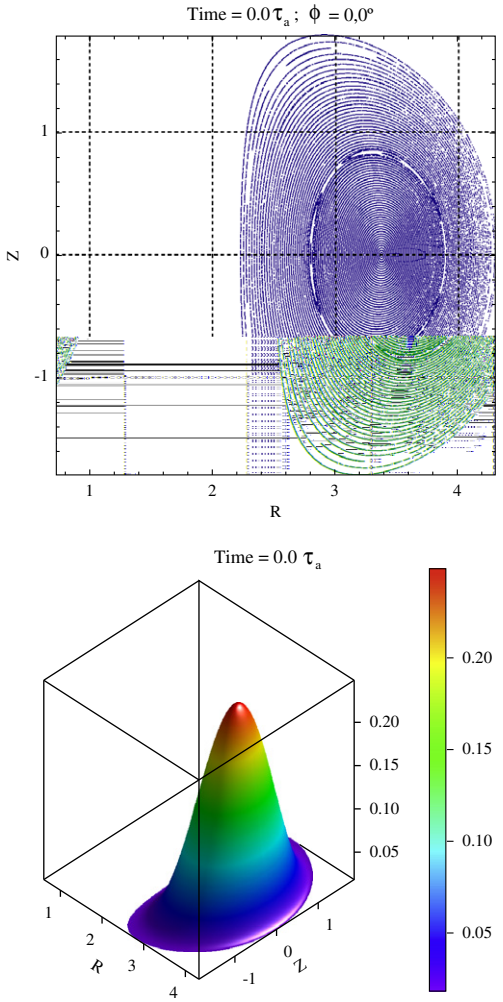

Fig. 9. $m/n = 3/2$ seed island used for the unstable case in Fig. 8. The seed island of the stable case is the same but rescaled by a factor 0.933.

or Edge Localized Modes (ELM's). However such a link has not yet been established by numerical simulations.

The XTOR simulation is performed with the resistive MHD model including thermal transport and the bootstrap current. The central plasma resistivity is $\eta_0 = 10^{-7}$ and the plasma viscosity $v = 10^{-7}$. The parallel and perpendicular transport coefficients are $\chi_{//} = 30$ and $\chi_{\perp} = 3 \times 10^{-7}$, respectively. The seed island is produced in a separate simulation by increasing f_{bs} in the bootstrap current or the resistivity in the plasma. It is then rescaled to perturb the linearly stable equilibrium.

In Fig. 8, the magnetic island size time evolution of a $m/n = 3/2$ NTM are shown for two simulations in the vicinity of its nonlinear stability threshold. The initial equilibrium has ITER [2] like characteristics, with an aspect ratio of $A = 3$, a plasma cross-section elongation $\kappa = 1.75$ and triangularity $\delta = 0.4$. The equilibrium q and pressure profile are the same as the shifted q-profile case in Refs. [26–28], but in the present case, only the dynamics of a single NTM is presented. The only difference between the stable (red) and the unstable (blue) case in Fig. 8[1] is the size of the initial seed island. Here, $w_{\mathrm{seed}}^{\mathrm{stable}}/w_{\mathrm{seed}}^{\mathrm{unstable}} = 0.93$ and the marginal seed island size it approximately $w_{-}/a = 3.1\%$.

[1] For interpretation of the references to color in this figure, the reader is referred to the web version of this article.

In Fig. 9, the Poincaré section of the magnetic field and the 3D view of the pressure of the perturbed equilibrium are shown. In Fig. 10, the same plots are presented at the end of the nonlinearly unstable case in Fig. 8. The plasma evolves towards a 3D equilibrium state with a saturated $m/n = 3/2$ island. In Fig. 11 however, the same plots are shown for the nonlinearly stable case in Fig. 8. The initial seed island vanishes on a resistive scale time until the initial unperturbed equilibrium is recovered.

The stable and the unstable cases in Fig. 9 were performed with 200 radial points, 12 toroidal modes (including $n = 0$) and every toroidal mode has a resolution of 32 poloidal modes. These simulations costed 4 and 10 hours cpu time at about 5 Gigaflops on one processor of a NEC SX8 vector computer for the stable and the unstable case in Fig. 9, respectively.

Typical time steps determined by the limiters of Section 3.4 range between $3\tau_a$ and $5\tau_a$ throughout all the simulation. A weak limitation comes from the radial magnetic field through the condition (18). Furthermore, the slow diffusion of the axisymmetric fields leads to about three violations of the condition (20) during the entire simulation thus resulting in three computations and decompositions of the semi-implicit matrices.

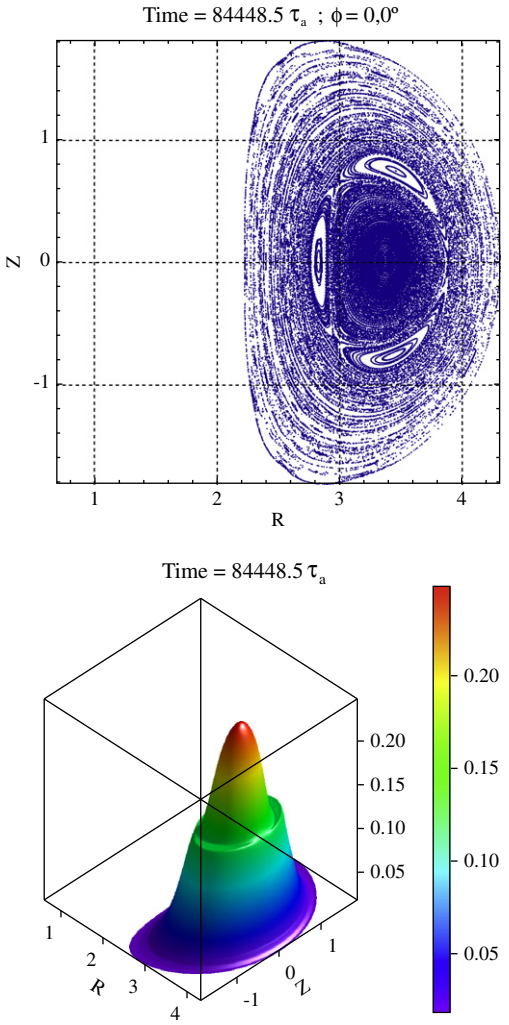

Fig. 10. Poincaré plot of the magnetic field and 3D view of the Pressure at the end of the unstable case in Fig. 8.

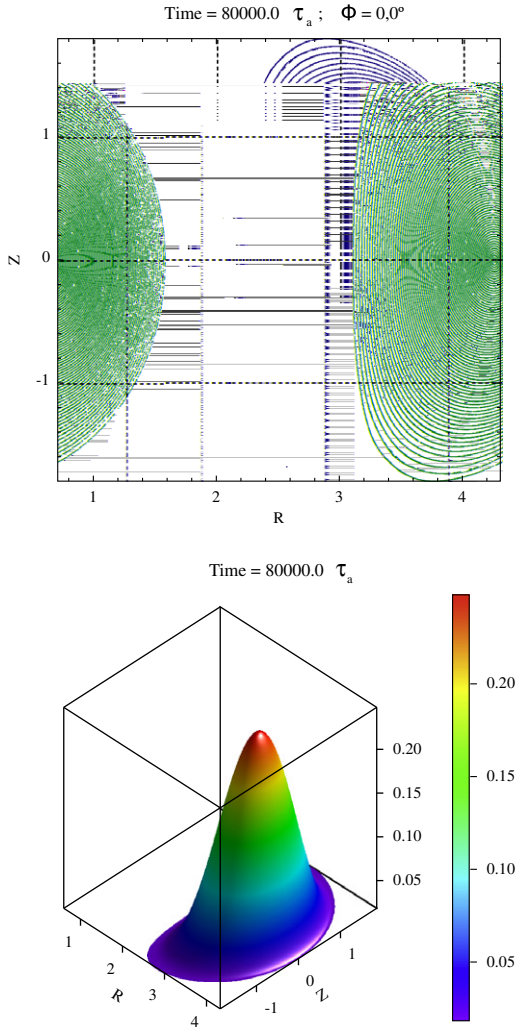

Fig. 11. Poincaré plot of the magnetic field and 3D view of the pressure at the end of the stable case in Fig. 8.

5. Discussion and perspectives

The semi-implicit time advance scheme used in the XTOR code has proven its robustness to solve the nonlinear evolution of internal instabilities in tokamak plasmas with an extended MHD model. For example, it can solve routinely the nonlinear evolution of a tearing instability with a plasma resistivity of $\eta_0 = 10^{-7}$ with a typical linear growth rate of the order of a few $10^{-5}\tau_a^{-1}$ and a total simulation time of a few $10^5\tau_a$, i.e. with a ratio of 10^{10} between the fastest and the slowest mode in the system. It was used to study the NTM dynamics in details [24–28] and is now regularly used to reproduce dynamics of experimental discharges, in particular in TORE-SUPRA [29,30] and JET [38]. Furthermore the code allows parameter studies because typical simulation times are of the order of 10 cpu hours with a NEC SX-8.

The most straightforward development of XTOR, keeping the same numerical scheme would be a coupling with a pseudo-vacuum region outside the plasma boundaries provided by the CHEASE code. As it would include a separatrix and X-points this region would be discretized by a finite element method. It could include the boundary conditions by a set of real magnetic coils. Such a tool could for instance be useful to assess MHD stability during all the life of the plasma in integrated plasma modelizations. However our main goal at present is the simulation beyond extended MHD in order to include kinetic, diamagnetic and fast particles

effects. For this purpose it is necessary to transform the semi-implicit numerical scheme into a fully implicit one for two reasons. The first one is that the semi-implicit method is well adapted for the solution of symplectic sets of equations such as ideal MHD. An extension to a bifluid model which is no more symplectic was developed, but the performance of the semi-implicit method turned out to be poor, and it was concluded that this is not the right way for future developments. Secondly, present computer capacities allow the fully implicit treatment of three-dimensional MHD. It appears that all the algebra and tools developed for XTOR in a long term work can be readily used with little work overhead. Such an implicit code using a Newton–Krylov method is currently under development, generalizing the work of Chacón et al. in reduced MHD [39]. Only the time advance must be replaced by an implicit one using Newton–Krylov solvers. This new implicit version of the code will be presented elsewhere after sufficient benchmarking.

Acknowledgments

This work was financed in part by the association EURATOM – CEA sur la fusion, Cadarache, Contract Nos. 2939 and 3530. The calculations were executed with the computing facilities of the Institut du Développement et des Ressources en Informatique Scientifique, CNRS, Orsay, France. We acknowledge Jean-Claude Adam and David Leblond for a careful reading of the manuscript. Most of the graphics were realized with the SmileLab software which can be found at http://www.satimage.fr/software/en/index.html.

References

[1] H. Lütjens, Comp. Phys. Commun. 164 (2004) 301.
[2] R. Aymar, V.A. Chuyanov, M. Huguet, et al., Nucl. Fusion 41 (2001) 1301.
[3] M.N. Rosenbluth, R.Y. Dagazian, P.H. Rutherford, Phys. Fluids 16 (1973) 1894.
[4] M.N. Bussac, R. Pellat, D. Edery, J.L. Soulé, Phys. Rev. Lett. 35 (1975) 1638.
[5] H.R. Strauss, Phys. Fluids 19 (1976) 134.
[6] W. Park, D.A. Monticello, R.B. White, S.C. Jardin, Nucl. Fusion 20 (1980) 1181.
[7] A.Y. Aydemir, D.C. Barnes, J. Comput. Phys. 53 (1984) 100.
[8] B.V. Waddell, M.N. Rosenbluth, D.A. Monticello, R.B. White, Nucl. Fusion 16 (1976) 528.
[9] H.R. Hicks, B. Carreras, J.A. Holmes, D.K. Lee, B.V. Waddell, J. Comput. Phys. 44 (1981) 46.
[10] R. Izzo, D.A. Monticello, H.R. Strauss, W. Park, J. Manickam, R.C. Grimm, J. DeLucia, Phys. Fluids 26 (1983) 3066.
[11] A.Y. Aydemir, D.C. Barnes, J. Comput. Phys. 59 (1985) 108.
[12] W. Park, D.A. Monticello, H.R. Strauss, J. Manickam, Phys. Fluids 29 (1986) 1171.
[13] A.M. Popov, V.S. Chan, M.S. Chu, Y.Q. Liu, B.W. Rice, A.D. Turnbull, Phys. Plasmas 8 (2001) 3605.
[14] D.S. Harned, W. Kerner, J. Comput. Phys. 60 (1985) 62.
[15] D.S. Harned, D.D. Schnack, J. Comput. Phys. 65 (1986) 57.
[16] D.D. Schnack, D.C. Barnes, Z. Mikic, D.S. Harned, E.J. Caramana, J. Comput. Phys. 70 (1987) 330.
[17] L.A. Charlton, J.A. Holmes, V.E. Lynch, B.A. Carreras, T.C. Hender, J. Comput. Phys. 86 (1990) 270.
[18] K. Lerbinger, J.F. Luciani, J. Comput. Phys. 97 (1991) 444.
[19] C.R. Sovinec, A.H. Glasser, T.A. Gianakon, D.C. Barnes, R.A. Nebel, S.E. Kruger, D.D. Schnack, S.J. Plimpton, A. Tarditi, M.S. Chu, J. Comput. Phys. 195 (2004) 355.
[20] H. Baty, J.F. Luciani, M.N. Bussac, Phys. Fluids B 4 (1993) 1213.
[21] H. Lütjens, A. Bondeson, A. Roy, Comput. Phys. Commun. 69 (1992) 287.
[22] H. Lütjens, A. Bondeson, O. Sauter, Comput. Phys. Commun. 97 (1996) 219.
[23] H. Lütjens, J.F. Luciani, Phys. Plasmas 4 (1997) 4192.
[24] H. Lütjens, J.F. Luciani, X. Garbet, Phys. Plasmas 8 (2001) 4267.
[25] H. Lütjens, J.F. Luciani, X. Garbet, Plasma Phys. Control. Fusion 43 (Suppl. 12A) (2001) A339.
[26] H. Lütjens, J.F. Luciani, Phys. Plasmas 9 (2002) 4837.
[27] H. Lütjens, J.F. Luciani, Phys. Plasmas 12 (2005) (Art. no. 080703).
[28] H. Lütjens, J.F. Luciani, Phys. Plasmas 13 (2006) (Art. no. 112501).
[29] P. Maget, H. Lütjens, G.T.A. Huysmans, P. Moreau, B. Schunke, J.L. Segui, X. Garbet, E. Joffrin, J.F. Luciani, Nucl. Fusion 47 (2007) 233.
[30] P. Maget, G.T.A. Huysmans, X. Garbet, M. Ottaviani, H. Lütjens, J.F. Luciani, Phys. Plasmas 14 (2007) (Art. no. 052509).
[31] O. Sauter, R.J. La Haye, Z. Chang, et al., Phys. Plasmas 4 (1997) 1654.
[32] C. Angioni, O. Sauter, Phys. Plasmas 7 (2000) 1224.
[33] G. Bateman, MHD Instabilities, The MIT Press, Cambridge, Massachusetts and London, England, 1978, ISBN 0-262-021131-5.
[34] W.H. Press, B.P. Flannery, S.A. Teukolsky, W.T. Vettering, Numerical Recipes, The Art of Scientific Computing, Cambridge University Press, Cambridge, 1990, p. 386.

[35] W. Park, E.D. Fredrickson, A. Janos, J. Manickam, W.M. Tang, Phys. Rev. Lett. 75 (1995) 1763.
[36] H. Lütjens, J.F. Luciani, in: Proceedings of the 1998 International Congress on Plasma Physics combined with the 25th EPS Conference on Controlled Fusion and Plasma Physics, June 29–July 3, 1998, Praha, Czech Republic, p. 2042.
[37] Z. Chang, J.D. Callen, E.D. Fredrickson, R.V. Budny, C.C. Hegna, K.M. McGuire, M.C. Zarnstorff, the TFTR Group, Phys. Rev. Lett. 74 (1995) 4663.
[38] N. Schaeffer, P. Maget, H. Lütjens, G.T.A. Huysmans, the JET EFDA contributors, in: Proceedings of the 34th EPS Conference on Plasma Physics and Controlled Fusion, July 2–6 2006, Warsaw, Poland, in press.
[39] L. Chacón, D.A. Knoll, J.M. Finn, J. Comput. Phys. 178 (2002) 15.